ELSEVIER

Journal of Fluids and Structures 22 (2006) 3–19

JOURNAL OF FLUIDS AND STRUCTURES

www.elsevier.com/locate/jfs

Buffeting of large telescopes: Wind-tunnel measurements of the flow inside a generic enclosure

T. Pottebaum[a], D.G. MacMynowski[b,*]

[a]*Aerospace and Mechanical Engineering Department, University of Southern California, Los Angeles, CA 90089, USA*
[b]*Department of Control and Dynamical Systems, California Institute of Technology, 1200 E. California Blvd., M/C 104-44 Pasadena, CA 91125, USA*

Received 8 October 2004; accepted 3 August 2005
Available online 7 October 2005

Abstract

The design of future large optical telescopes must take into account the wind-induced vibration of the telescope structure that is caused by large-scale flow structures and turbulence inside the telescope enclosure when the aperture in the enclosure dome is open. However, estimating the resulting degradation in image quality is difficult due to our relatively poor understanding of the flow inside the enclosure. Data has been collected in a wind-tunnel test of an empty telescope enclosure to understand the flow-field around the region near the dome opening where the secondary mirror and supporting structure would be subjected to wind loads. Digital particle image velocimetry (DPIV) data was collected in a vertical plane near the dome opening to obtain mean velocity and fluctuation kinetic energy, and hot-wire data was collected along the telescope axis to obtain temporal spectra of the velocity. Data was collected both with and without additional venting, in order to understand its influence on the flow. The temporal spectrum of the broadband turbulence is of von Karman type. The flow field also includes tonal shear layer modes, with the mode selection influenced by the enclosure Helmholtz mode, and the overall amplitude strongly influenced by the vented area. In addition to its direct use in telescope modelling and design, the data presented herein is of particular value in validation of computational fluid dynamic (CFD) analyses, so that CFD can be used with confidence in future design work.

Keywords: Telescope; Dome; DPIV; Venting; Wind-tunnel

1. Introduction

The enclosure surrounding a ground-based optical telescope provides a significant reduction in the wind loads on the telescope structure. However, with the aperture open, the residual wind loads resulting from large scale flow structures and turbulence inside the telescope enclosure may still lead to significant vibration that must be taken into account in the design of future large telescopes (Padin and Davison, 2004; Angeli et al., 2004; MacMynowski et al., 2004), affecting the design of the enclosure, the structure and the control system. To estimate the resulting image degradation with sufficient confidence for design, a better understanding of the wind inside the telescope enclosure is required. There is currently very little data on the flow characteristics; measurements in existing telescopes are expensive and therefore

*Corresponding author.
E-mail address: macmardg@cds.caltech.edu (D.G. MacMynowski).

0889-9746/$ - see front matter
doi:10.1016/j.jfluidstructs.2005.08.005

limited, and prior wind-tunnel tests have also recorded only limited data. However, progress in wind-tunnel measurement techniques now allows us to collect much more information about the flow than was previously possible, allowing a better understanding of the loads that the telescope structure will be subjected to for use in modelling and design.

Wind loads are relevant both over the primary mirror (M1) and on the secondary mirror (M2) and nearby supporting structure. Typical locations for these mirrors relative to the enclosure are shown in Fig. 1. Although the cross-sectional area of M2 is small compared to that of M1, the structure around the mirror is exposed to higher wind loads, and thus the resulting forces may be the more significant contributor to image degradation (Padin and Davison, 2004), both directly through the motion of M2, and through the deformation of M1 via coupling through the structure. Steady forces can be compensated for by active control of the telescope structure. Estimates of the unsteady forces, however, require knowledge of the unsteady wind velocity. The resulting optical consequences can then be computed from an integrated model that predicts the actively controlled structural response (Angeli et al., 2004). For design purposes, it is essential to understand not only the wind speed or pressure at a few isolated locations, but more details of the flow pattern that can be used, for example, to help choose the clearance between M2 and the dome. In addition, future telescope enclosures are likely to incorporate additional vent openings to permit continual air circulation around M1 in order to maintain thermal equilibrium. In wind conditions where buffeting is of concern, the total vented area would be small, but may still influence the flow pattern around M2.

An understanding of the wind inside a telescope enclosure can be obtained from various sources, including measurements in observatories (Forbes and Gabor, 1982; Cho et al., 2002; Angeli et al., 2002), computational fluid dynamics (CFD) (DeYoung, 1996; Vogiatzis et al., 2004) or through wind- or water-tunnel experiments (Kiceniuk and Potter, 1986; Schneermann, 1994; Riewaldt et al., 2004; Fitzsimmons et al., 2004). While full-scale tests are ideal, limited data is available both because of the expense and because of the difficulty in controlling test conditions. Forbes and Gabor (1982) measured pressure at only a few points inside the MMT dome, while the data collected at Gemini South Observatory (Cho et al., 2002) includes many pressure measurements over the primary mirror and a few velocity measurements, but is still insufficient for either design purposes or CFD validation, particularly for the flow near M2. Because of the time-varying three-dimensional nature of the flow, CFD simulations are computationally intensive. Furthermore, some experimental data is still required in order to validate CFD results before CFD can be used with confidence in future design work. Only flow visualization or limited data at a few points inside the telescope enclosure is available from the older wind-tunnel tests. More recently, Fitzsimmons et al. (2004) have reported pressure data at 36 locations across M1 using a dome geometry similar to ours; their results are complementary to the experiment described herein, which provides more information on the flow patterns near M2. Newer experimental techniques such as digital particle image velocimetry (DPIV) allow us to collect significantly more data about the flow field inside the telescope enclosure than prior tests, leading to both a better understanding of the flow field, and quantitative information that can be used in modelling and design. In addition to its direct use in telescope modelling and design, the experimental data is of particular value in validation of CFD analyses.

Data has been collected in a scaled wind-tunnel test of a telescope enclosure to understand the flow-field around the region near the dome opening where M2 and its supporting structure would be subjected to wind loads. The test geometry used herein is shown in Figs. 2 and 3; note that the telescope itself is not included, so that the test results are not specific to a particular choice of telescope design parameters. For high external wind speeds where wind-buffeting

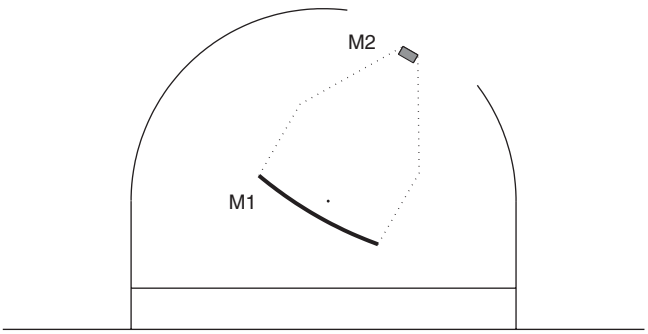

Fig. 1. Cross-sectional schematic of telescope enclosure showing representative locations of the primary mirror (M1), secondary mirror (M2) near the enclosure opening, and the secondary mirror support structure (shown dotted). Additional structure would exist behind and beside the primary mirror. Geometry shown is for a 30 m f/1.5 primary below the elevation axis ('·') and 3.5 m Ritchey–Chretien secondary, mounted in an 84 m diameter dome.

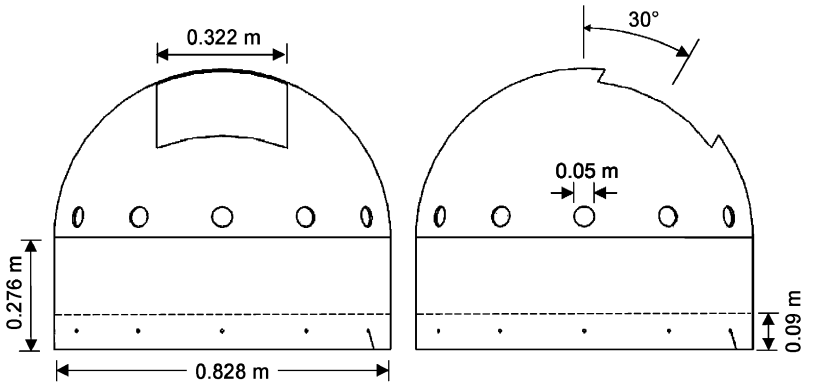

Fig. 2. Front and side view of scale telescope enclosure model used in wind-tunnel testing. The 12 vent holes shown could be covered for baseline testing of an unvented enclosure.

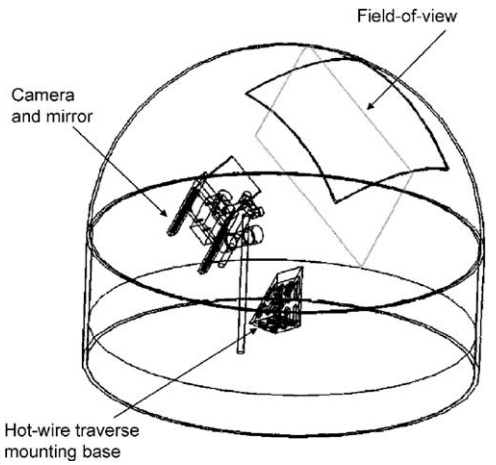

Fig. 3. Isometric view of wind-tunnel model showing location of camera and mirror, image plane for DPIV data, and the mounting point for hot-wire traverse.

may be an issue, the full-scale Reynolds number of the flow is sufficiently high so that the full-scale flow throughout the telescope enclosure is turbulent. To be meaningful, the experimental Reynolds numbers must therefore be sufficiently high to ensure that the flow is also turbulent. The model is intended to be representative of a generic empty telescope dome at approximately 1% of the expected full-scale enclosure size for a 30 m diameter telescope. The elevation angle of the square dome opening was fixed at 30° from zenith, and any azimuth angle could be tested. In addition, vent holes were cut in the model (see Fig. 2 for geometry) with a total cross-sectional area equal to 25% of the dome opening area, and data was collected with all of these closed, half open, and all open.

Flow visualization was used to determine the general flow patterns in the enclosure. DPIV data was then collected in a vertical plane near the dome opening to obtain mean velocity and fluctuation kinetic energy information. This technique provides a detailed, quantitative, two-dimensional spatial "map" of the velocity information that is extremely valuable both for understanding the flow field and for validating computational results, but the data cannot be recorded at a sufficient rate to give spectra. Hot-wire data was therefore collected along the telescope axis to obtain temporal spectra of the velocity at discrete points. The DPIV data was collected only for azimuth angles of 0° and 180° with respect to the wind, so that the mean flow along the center-line remained planar due to symmetry.

In addition to the mean circulation pattern within the enclosure, the unsteady flow includes both broadband turbulence and large-scale structures associated with shear layer modes over the dome opening. The measured spectrum of the broadband turbulence inside the telescope enclosure is found to be close to a von Karman spectrum, consistent with previous telescope wind-tunnel tests (Ravensbergen, 1994) and full-scale measurements (Angeli et al., 2002).

The shear layer modes occur as a result of feedback from the downstream edge of the opening interacting with the separation off the upstream edge to organize the vorticity into distinct modes (Rossiter, 1964). These modes are also present in computational and experimental analysis of "clean" dome configurations (Srinivasan, 2000; Vogiatzis et al., 2004; Fitzsimmons et al., 2004). In addition to characterizing these modes for the telescope enclosure geometry, one of the conclusions of this paper is that the presence of open vents significantly decreases the amplitude of these modes.

The experiment and data collection approach are described in the next section. Representative data to illustrate the general flow characteristics are presented in Section 3 for both the unvented and vented enclosure, including both temporal spectra and the spatial distribution of wind speeds. The shear layer modes and their dependency on test conditions are discussed in more detail in Section 5. Finally, the implications on telescope wind loads are discussed in Section 6.

2. Experimental approach

2.1. Scaling

Several important parameters must be scaled properly in order for this set of experiments to be related to a full-scale telescope. In particular, the Reynolds number of the flow and the scaling of frequencies must be considered.

The Reynolds number is defined as

$$\mathrm{Re} = \frac{U_\infty D}{\nu}, \tag{1}$$

where U_∞ is the freestream velocity, ν is the kinematic viscosity, and D is the characteristic length scale, taken here to be the enclosure diameter. This ratio represents the relative importance of inertial forces to viscous forces in the momentum balance for a flow. High Reynolds number flows are typically turbulent, although the critical Reynolds number for turbulence depends on the type of flow. Our wind-tunnel model is roughly 1% of full scale, but the speeds used in the test are roughly 3 times as large as those of interest for telescope design, leading to roughly 3% of the full-scale Reynolds number. This is sufficient to ensure turbulent flow in the region near the secondary mirror where data was collected. Information regarding loads on M1 are harder to obtain in wind-tunnel testing, because the decrease in wind speeds further inside the telescope enclosure makes it more difficult to ensure that the flow remains turbulent.

There are two relevant time scales or frequencies associated with the flow. First, the convective time scale of flow across the dome opening is relevant both in the convection of periodically occurring large scale structures in the flow, and for determining the outer scale of Kolmogorov turbulence. The convective frequency is proportional to

$$f_0 = \frac{U_\infty}{L}, \tag{2}$$

where L is the aperture dimension. Acoustic phenomena are also relevant for this flow field, with the important scaling parameter being the Helmholtz resonance of the telescope enclosure. While the "neck" length of the dome opening is zero, including the added mass from air around the opening gives a frequency

$$f_H = \frac{c\mu}{2\pi}\sqrt{\frac{L}{V}}, \tag{3}$$

where c is the speed of sound, V is the enclosed volume, and $\mu = (\sqrt{\pi}/1.7)^{1/2} \simeq 1$ accounts for the end effects (Beranek, 1954). As with f_0, this frequency scales inversely with the length scaling of the model. However, the Helmholtz frequency scales with the speed of sound while the convective frequency scales with the flow speed. Thus by increasing the flow speeds used in the wind-tunnel experiment relative to the expected mountain-top speeds in order to better match the Reynolds number, we have changed the ratio f_0/f_H, and must take this into account when interpreting results.

2.2. Test facility

The experiments were carried out in the Lucas adaptive wall wind-tunnel (AWT). This facility uses adaptive wall technology in the test-section to reduce the wall effects typical of straight-wall wind-tunnel tests (Lamarche and Wedemeyer, 1984; Sears and Erickson, 1988), allowing for a larger model to be tested relative to the test-section cross-section. Pressure measurements along the length of the test-section floor and ceiling are used to determine the wall contour that will result in the wall following a streamline for the current model configuration. With the test-section

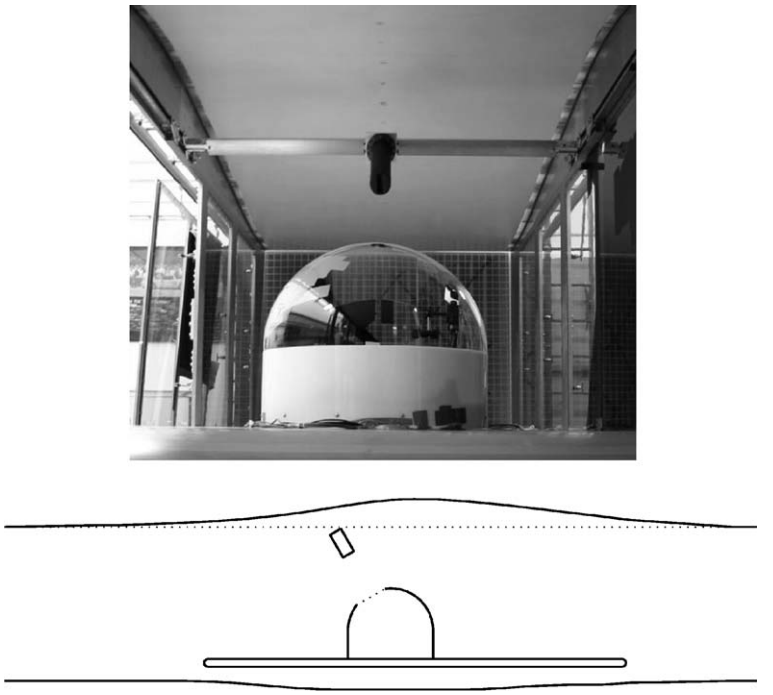

Fig. 4. Picture of enclosure model inside the Lucas adaptive wall wind-tunnel (upper) and schematic (lower), illustrating the deformation of the ceiling. The pressure taps along the ceiling that are used to define the desired upper wall contour can be identified in the picture. The crossbar supports the beam-spreading optics used for DPIV measurements.

ceiling and floor deformed to the desired contour, the flow pattern resembles that of an infinite flow field, rather than one confined by the walls of the tunnel.

The test-section of the Lucas AWT is 7.62 m long and has a rectangular cross-section 1.83 m wide and 1.52 m high when un-adapted. The ceiling and floor each have a maximum displacement of 0.30 m away from the mid-plane of the tunnel. A rigid ground plane equipped with a yaw table was installed in the test-section to support the telescope enclosure model. With the ground plane installed, the test-section floor is used to control the location of the leading edge stagnation point on the ground plane, and only the ceiling is used to adapt for the model. Over a wide range of flow speeds, the required wall deflection at each streamwise location is nearly equal to the cross-sectional area of the model at that location, leading to a maximum allowable model cross-sectional area of $0.56\,m^2$. A picture and schematic of the enclosure model (described in the next section) mounted on the ground plane inside the Lucas AWT is shown in Fig. 4, clearly showing the deformed ceiling as well as the pressure taps used in the adjustment algorithm.

2.3. Enclosure model

In order to obtain data useful for design purposes, a generic telescope enclosure design is considered, and no telescope structure is included inside the enclosure. While the presence of the telescope would clearly affect the flow near the primary mirror, the cross-sectional area of M2 is small compared to that of the dome opening and therefore is not likely to significantly affect the large-scale flow patterns. The full-scale enclosure is taken to consist of a 90 m diameter hemisphere placed upon a 30 m tall right cylinder with the same diameter. Inside the enclosure is a floor that is placed 10 m above the base of the cylinder. All walls have a thickness of 1 m, and the enclosure aperture is modelled as a square opening whose sides measure 35 m. Twelve 5.5 m diameter vent holes are equally spaced around the azimuth, 7° above the bottom of the hemisphere, to give a total possible vented area equal to 25% of the area of the dome opening. Only the area and approximate distribution of the vents, and not the details of the vent geometry, are believed to be significant for influencing the flow near M2, and thus this geometry was chosen for ease of testing and CFD simulation.

The wind-tunnel model, shown in Fig. 2, consisted of a 0.83 m diameter hemisphere of clear acrylic plastic mounted on a 0.28 m tall right cylinder with the same diameter. The cylinder portion of the model had a wall thickness of 9.5 mm.

The hemisphere portion wall thickness varied due to the manufacturing process, with a maximum thickness of 9 mm where it attached to the cylinder and a minimum thickness of 5 mm at the zenith. A square with side length 0.32 m was removed from the hemisphere at an elevation of 30° from zenith. A 0.09 m thick cylindrical wooden base with diameter matching the interior diameter of the acrylic cylinder was attached to the center of the ground plane yaw table and the acrylic model attached to the wooden base. The azimuth angle of the model aperture was varied by rotating the yaw table, with 0° azimuth corresponding to the aperture facing directly into the wind.

2.4. Experimental techniques

Smoke and tufts were used to visualize the flow pattern in and around the enclosure model. Smoke injected into the flow at a known location produces qualitative information about the large scale structures in the flow and the general circulation pattern of the flow by observing how the smoke particles are convected. Tufts of string attached to the surface are oriented by the shear stress produced by the flow, giving an indication of the direction of the flow, and a qualitative sense of the flow unsteadiness based on whether the tufts vibrate or remain pointed in one direction.

Temporal spectra of the unsteady flow velocity were obtained from hot-wire measurements. A hot-wire anemometer measures fluid velocity by sensing changes in heat transfer from a small, electrically heated sensor (hot-wire) exposed to the flow. A feedback circuit maintains the hot-wire sensor at a constant temperature, and the current needed to keep the temperature constant is directly related to the heat transfer from the flow past the hot-wire, and thus to the flow velocity. Hot-wires are particularly useful for measurements of unsteady velocities due to the high-frequency response that can be obtained. They are sensitive primarily to the flow component orthogonal to the wire and less sensitive to the flow component along the wire direction. The velocity estimates are therefore most reliable when the flow velocity is known to be in the plane orthogonal to the wire. In this experiment, the hot-wire is placed so that it is most sensitive to flow in the (vertical) plane of symmetry of the model, and less sensitive to flow in the spanwise direction. Due to symmetry, therefore, the flow is in the plane orthogonal to the wire when the enclosure azimuth angle with respect to the wind is either 0° or 180°. The relationship between flow speed u and the output voltage V is approximately $V^2 = A + Bu^n$. The hot-wire data are used to understand the frequency spectrum, with quantitative information about the mean and unsteady flow field available from DPIV data. For sufficiently small perturbations in the voltage, the perturbation in velocity is proportional to the perturbation in voltage, and the spectral characteristics can be obtained up to an unknown scale factor in the absence of an accurate calibration. Since $n \simeq 0.5$, pertubations in V^4 were computed in order to increase the range over which the scale factor would remain constant.

Detailed spatial information was obtained using DPIV; a technique for determining the in-plane velocity field in a cross-section of a flow (Willert and Gharib, 1991). Experiments are typically carried out by seeding the flow with reflective or fluorescent particles, illuminating a thin cross-section of the flow field with pulsed monochromatic light, and capturing images of the particles using a CCD video camera. Displacement estimates are obtained by locating the peak of the cross-correlation of the intensity between small interrogation windows within pairs of consecutive images. This method of processing depends on the particles within the interrogation window primarily being convected by the flow, rather than large velocity differences existing within the window. The displacements are then converted to velocities using the known time separation between pulses of the light source. Many refinements of the original DPIV processing technique have been developed. In particular, window-shifting reduces the effect of particles entering and leaving an interrogation window between images by relocating the interrogation window in the second image based upon an initial displacement estimate without window-shifting. A variety of different processing techniques are currently in use, each with its own strengths and weaknesses (McKenna and McGillis, 2002).

2.5. Experimental set-up

A hot-wire probe (model 1210; TSI Incorporated, Shoreview, MN, USA) was mounted on a motorized traverse inside of the model. The traverse was aligned with the model such that the probe could be moved along the nominal telescope axis (i.e., the line connecting the spherical center of the hemisphere and the center of the aperture). For all azimuth angles, the hot-wire probe was oriented to measure the magnitude of the velocity in the vertical plane containing the nominal telescope axis. In addition, at 90° azimuth the probe was oriented to measure velocities in the plane normal to the telescope axis. The sensing element of the hot-wire probe was a cylindrical element 1.3 mm in length and 3.2 μm in diameter. The hot-wire probe used an anemometer manufactured in-house at GALCIT, with the output recorded to computer through an analog-to-digital converter.

Imaging for both smoke visualization and DPIV data used a high-resolution CCD video camera (model CV-M4 + CL; JAI PULNiX Inc., Sunnyvale, CA, USA) with an 8 mm focal length lens, positioned inside the model along

with a mirror to image a region of the vertical plane on the model center-line containing the enclosure aperture. The center of the top of the field-of-view was tangent to the removed portion of the hemisphere at the middle of the aperture. A physical area of approximately 0.38 m × 0.30 m was imaged onto 1280 × 1024 pixels. The positions of the camera and mirror, the camera field-of-view, and the mounting base for the hot-wire traverse are shown in Fig. 3. Cabling for the camera, hot-wire and traverse exited the model through a hole in the wooden base and an opening in the yaw table. The cables then exited the wind tunnel through the pressure matching gap at the downstream end of the test-section.

A pair of frequency doubled Nd:YAG lasers (Gemini- PIV; New Wave Research Inc., Fremont, CA, USA) was used to generate a vertical light sheet along the center-line of the test-section. The laser heads were located outside of the test-section, and the light entered the test-section though an approximately 10 mm diameter hole in the sidewall. Beam turning and sheet forming optics were suspended from a streamlined crossbar mounted to the two test-section sidewalls near the ceiling. The optical elements and their associated translation and rotation stages were housed inside a streamlined fairing with openings to allow the laser beam to enter and the laser sheet to exit.

Water droplets were used as the seeding particles for DPIV. The droplets were produced by four fuel-injection type nozzles connected to the building water supply, giving a mean droplet diameter less than 100 μm. Three of the nozzles were located inside the enclosure model. The fourth nozzle was located on the upstream exterior surface of the model, just above the point on the center-line where the hemisphere and cylinder sections are joined. The mean droplet diameter was determined directly from the DPIV images by computing the number of illuminated pixels for each droplet and comparing the resulting distribution with the relative probabilities computed as a function of droplet size. The sub-pixel size estimate is then corrected for the point-response-function of the lens using Eqs. (5) and (6) from Adrian (1991).

DPIV images were recorded directly to computer hard disk. Laser pulse timing was controlled using a delay generator (model DG535; Stanford Research Systems, Sunnyvale, CA, USA) triggered by the camera Exposure Enabled output.

2.6. Experimental conditions and procedures

Most of the data was collected at a freestream speed of 35 m s^{-1} in order to achieve the highest possible Reynolds number without causing damage to the model. This speed was reproduced between separate runs to within 0.05 m s^{-1}. Additional tests were carried out at 19 and 28 m s^{-1}. The wind-tunnel test-section ceiling was adapted to the model shape before beginning data collection. The air temperature in the wind tunnel was typically 22 °C, and the freestream pressure was 101 kPa. The freestream turbulence intensity in the wind tunnel is estimated to be approximately 1% of the freestream velocity. Tests were conducted with all of the vent holes covered, half of the vent holes open, and all open. The data with half the vents open used alternate vents, with the vent located directly under the aperture closed. Unvented data was collected both before the vent holes were cut in the model, and with the vent holes cut but covered, to ensure that this did not affect the flow.

Smoke visualization was carried out for 0° and 180° azimuth angles at 35 m s^{-1} using a smoke wand upstream of the enclosure model. The smoke was illuminated with a pulsed sheet of laser light along the center-line of the tunnel. Images were recorded using the camera inside of the enclosure and a tripod mounted video camera outside of the wind tunnel. The smoke visualization images were used to examine large scale structures in the flow near the aperture. In addition, tufts were used for the 0° and 180° azimuth angle cases. Strips of tufts were located at four locations on the interior of the cylindrical section of the enclosure and at four locations on the raised floor. Handheld video camera footage was taken of the tufts and was used to determine the general flow pattern in the enclosure.

Hot-wire data was acquired for enclosure azimuth angles between 0° and 180° in 30° increments at 35 m s^{-1}. Additional hot-wire data was acquired for 0° and 90° azimuth angles at 19 and 28 m s^{-1}. Data was collected along the nominal telescope axis at 20 equally spaced locations between 45% and 103% of the hemisphere's radius. At each location, the control circuit output voltage was recorded for 3 s at a 30 kHz sampling rate. The power spectral density (PSD) of each time series was computed using Welch's modified periodogram method with a Hanning window with 15 000 samples and no overlap. Due to a faulty electrical connection discovered after data was acquired, a complete calibration was not obtained. Because the perturbations in the voltage are small compared to the absolute voltage, the relationship described earlier is sufficient to produce useful information about the velocity spectrum. Neither the scale factor on the spectrum nor the mean velocity can be computed, and thus the hot-wire data cannot be directly compared with DPIV data. Furthermore, unless the mean voltage and thus the calibration remain constant, the scaling between the spectra for different cases will differ. Nonetheless, as quantitative data is available from the DPIV data, the hot-wire data is only needed to understand the temporal spectrum of the unsteady velocity, and the absence of calibration does not impact the resulting understanding except in an accurate comparison of spectral amplitudes between different cases.

DPIV data was acquired for the 0° and 180° azimuth cases at $35\,\mathrm{m\,s^{-1}}$. Before acquiring DPIV data, the hot-wire probe and traverse were removed from the model to eliminate a source of reflections. Images were digitally recorded at a rate of 24 frames per second with a pixel depth of 10-bits. Due to the large difference in velocities inside of the model and outside of the model, it was not possible to select a pulse separation time that resulted in optimal particle displacements in all portions of the field-of-view. The time between laser pulses within an image pair was 200 μs for the 0° case and 300 μs for the 180° case in order to obtain reasonable results throughout the field-of-view. A total of between 2400 and 2500 pairs of images was obtained and processed to generate velocity field estimates for each case. The DPIV data was collected in a series of short runs because water droplets collected on the mirror and camera lens.

Before extracting velocity field measurements from the DPIV data, the images were preprocessed. First, the two least significant bits in the recorded images were dropped, resulting in 8-bit images compatible with existing processing software. Then, optical distortion introduced by the short focal length camera lens was removed using a mapping obtained from calibration images of a regular grid of points. Next, stationary features in the images, such as reflections from the model surface, were identified by forming averages of all of the data images. Two average images were formed for each case, one from all of the even frames and the other from all of the odd frames. This was done in order to account for possible differences in the illumination between even and odd frames. The large number of individual images in the averages guaranteed that only persistent, stationary features exist in the average images. The appropriate average image was then subtracted from each data image.

Velocity field data was extracted from the preprocessed images using 64×64 pixel interrogation windows with 75% overlap of adjacent windows for both cases. The large window size was necessary due to the large displacements in the region of flow outside of the model. Displacements were first estimated by cross-correlating the same region in both images of a pair. After removing outliers based on velocity magnitude and the overlap of adjacent interrogation windows, this displacement field was used to shift the interrogation window in the second image for use in a second cross-correlation. Outliers were removed from this second displacement field. The vector field was then smoothed to be consistent with the window overlap, and the displacements were converted to velocities. For the 180° case, an additional processing step was included to refine the velocity estimates to 32×32 pixel interrogation windows with 50% overlap. This analysis gives a two-dimensional map of the mean and root mean square (r.m.s.) fluctuation velocity with a spatial resolution of roughly 5 mm.

2.7. Experimental errors

Only the spectra of the hot-wire data are reported, and not the actual velocities. Over the range of frequencies and wind-tunnel speeds considered herein, the electrical noise on the signal is negligible (roughly one part in 10^6 based on measurements at zero velocity).

The DPIV data includes both random and systematic errors in the displacement estimates (note that the time interval between snapshots is controlled to approximately one part in 10^8 and is not a significant source of error in the velocity estimates). The random errors are typically less than one pixel, and after averaging over 2400 image pairs leads to a negligible error in the mean velocity of about $0.01\,\mathrm{m\,s^{-1}}$ or $0.014U_\infty$ at $35\,\mathrm{m\,s^{-1}}$. The r.m.s. velocity fluctuations reported include the effect of the random errors in addition to the true fluctuations, with the former leading to a uniform fluctuation field of r.m.s. $0.014U_\infty$ at $35\,\mathrm{m\,s^{-1}}$; this is several times smaller than the smallest fluctuation levels measured herein.

The systematic errors in the DPIV data can be more significant. There are two possible sources of error: particle loss/gain, which is well accounted for in the processing, and particles not following the flow. This latter source is the most significant source of uncertainty in the results, particularly in regions of high accelerations such as vortices and very close to the dome opening. The particle Reynolds number is sufficiently small so that Stokes' law may be used to estimate the drag coefficient on the particle, and the velocity error v_e can be computed from the measured particle acceleration $|\dot{v}_p|$ using Eq. (19) in Adrian (1991):

$$|v_e| = \frac{\rho_p d_p^2}{36\rho\nu}\,|\dot{v}_p| \tag{4}$$

for particle diameter d_p, particle and air densities ρ_p and ρ, and air viscosity ν.

For upwind orientations, the flow is accelerating throughout most of the DPIV field-of-view, and thus the velocity will be slightly under-estimated. Over most of the field-of-view, the errors are small ($<1\,\mathrm{m\,s^{-1}}$, or $<0.03U_\infty$). Larger errors exist in a narrow portion of the field-of-view very close to the dome opening, and this must be taken into account in interpreting the results. While this does not significantly affect the ultimate use of this data for the prediction of loads on the support structure for the secondary mirror, the flow velocity near the secondary mirror itself may be

underestimated by as much as 25%; this still represents a significant improvement in our understanding of the flow field near M2. For downwind orientations, the flow acceleration is much lower and the resulting velocity errors are small everywhere. Significant flow accelerations will also occur in vortices that occur in the shear layer (described in the subsequent section). The shear layer will appear in the DPIV data at the proper location and with the correct mean boundary velocities. However, the measured mean profile will be sharper than in the actual flow, while the measured fluctuations will lead to an apparently thinner shear layer than the actual flow.

3. General flow characteristics

As noted earlier, the unsteady flow includes both broadband turbulence and large-scale structures associated with shear layer modes over the dome opening. The general characteristics are obtained from flow visualization, spectra from hot-wire information, and quantitative spatial patterns from DPIV data.

At 0° azimuth, observation of the surface tufts indicate that the general flow inside the enclosure is down along the downstream surface, upstream and slightly upwards along the enclosure sides, and upward on the upstream surface. While the interior flow has some unsteadiness, there did not appear to be flow reversals. For the 180° case, the general flow inside the enclosure is down along the upstream surface, downstream and slightly upwards along the enclosure sides, and approximately stagnant on the downstream surface. The level of unsteadiness inside the enclosure is significantly lower for the 180° case than for the 0° case. These results are summarized in Fig. 5.

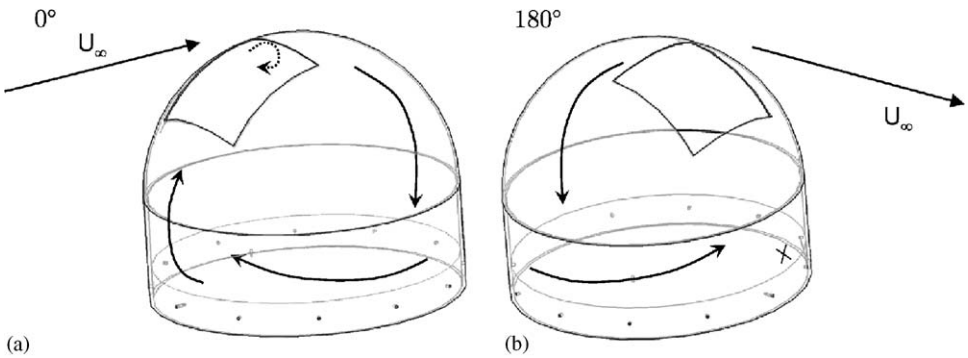

Fig. 5. Schematic of mean flow field obtained from tuft and smoke visualization for upstream (left; 0° azimuth) and downstream (right; 180° azimuth) orientation with respect to wind direction. Arrows indicate flow direction along the back of the enclosure, the sides, and the front ("×" indicating close to zero mean flow). The flow is symmetric, and only the flow on one side is shown for clarity.

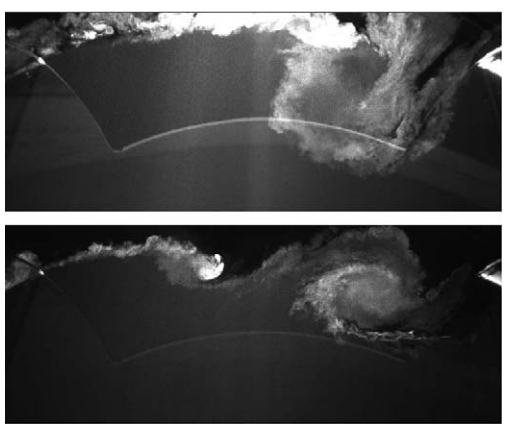

Fig. 6. Smoke visualization at two different freestream velocities showing different shear modes being excited; upper plot corresponds to 35 m s^{-1} where $n = 1$ mode is dominant, lower plot corresponds to 19 m s^{-1} where $n = 2$ mode is dominant. Images were taken with the camera inside the enclosure model and correspond to the top half of the field of view shown in Fig. 3.

At 0° azimuth, smoke visualization captures the repetitive roll-up of the shear layer over the aperture into large, unsteady vortices, shown in Fig. 6 for two different wind speeds. These vortices alternately travel into the enclosure, or are deflected upwards away from the enclosure along with the shear layer. Depending on the flow speed, there may be one or two vortices spanning the aperture at one time. For the 180° case, the smoke visualization did not reveal any large scale structures near the aperture.

Typical spectra, obtained using hot-wire measurements of velocity, are shown in Figs. 7 and 8. These figures correspond to a location at 96% of the dome radius; while the spectrum clearly changes with location, the general characteristics described below are similar for all locations. For all azimuth angles and all locations along the telescope axis, the PSD of the hot-wire data includes a broadband turbulence component that is consistent with a von Karman spectrum; i.e., proportional to $(f^2+f_S^2)^{-5/6}$ for some outer scale frequency f_S.

For azimuth angles $\leqslant 90°$ and for all locations along the telescope axis, the PSD also includes distinct peaks at multiples of approximately $0.62f_0$. A typical spectrum, for a 0° azimuth and a $35\,\mathrm{m\,s^{-1}}$ wind-tunnel speed, is shown in

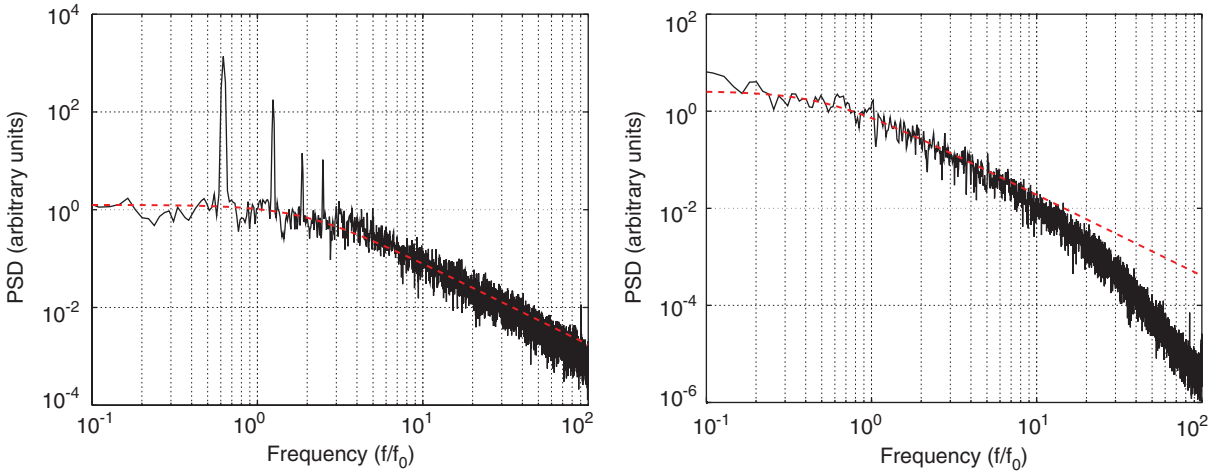

Fig. 7. Power spectrum (arbitrary scale) of unsteady velocity measured using hot-wire probe within the shear layer at $35\,\mathrm{m\,s^{-1}}$ freestream velocity. Lefthand and righthand plots correspond to 0° and 180° azimuth respectively with respect to the incoming wind. A von Karman turbulent spectrum is shown for comparison.

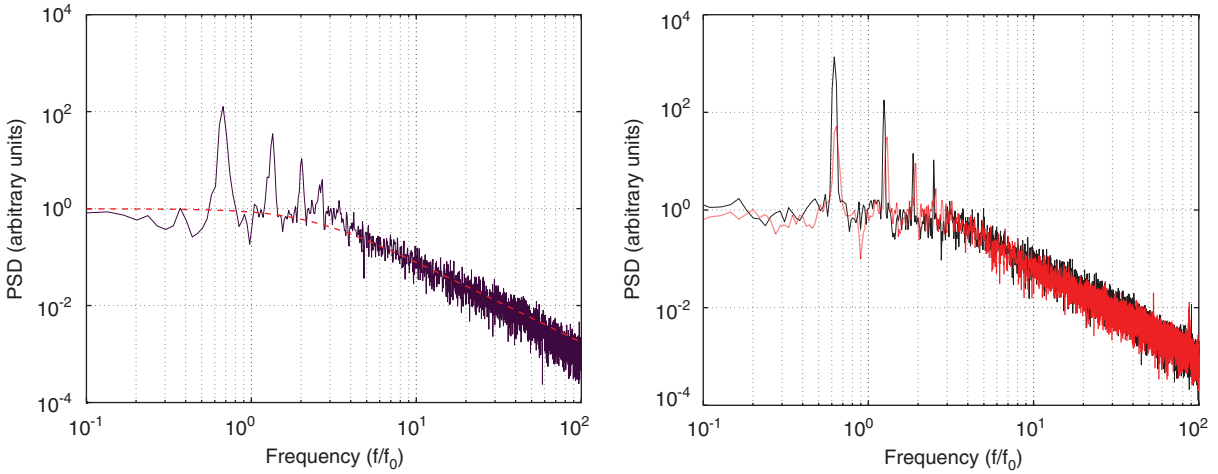

Fig. 8. Power spectrum of unsteady velocity within the shear layer, at a 0° azimuth with respect to the incoming wind. Lefthand plot shows spectrum at $19\,\mathrm{m\,s^{-1}}$ freestream velocity, with a von Karman turbulent spectrum shown for comparison. Righthand plot compares spectra at the same location for a $35\,\mathrm{m\,s^{-1}}$ freestream velocity without venting (solid) and with 6 vents open (red).

the left-hand plot of Fig. 7. At this location within the shear layer, roughly 90% of the mean-square velocity is associated with these peaks. The relative fraction of tonal versus broadband contributions to the mean-square decreases further inside the dome, but for this case remains above 50% for all locations. Fig. 7 also shows a typical spectrum for an azimuth angle $>90^\circ$ where there are no such peaks. The relative magnitudes of the frequency peaks depend upon the freestream velocity, while the nondimensional frequencies (normalized by the convective frequency f_0) are independent of velocity. This can be seen by comparing Fig. 7(a) with 8(a). Each of these PSD plots represents data taken at the same location and at the same azimuth angle, but at different freestream velocities. Note that the mean hot-wire voltage differs by roughly 5% between these two cases, which will change the calibration. Thus the absolute amplitudes cannot be accurately compared because of the absence of a hot-wire calibration; nonetheless the relative amplitude of the shear layer modes and broadband turbulence clearly changes. The next section describes these shear layer modes in more detail.

Figs. 9–12 show the mean and r.m.s. in-plane flow fields measured using DPIV for different cases, normalized by the freestream velocity. In each plot, the origin of the coordinate system is at the spherical center of the hemisphere (see Fig. 3), with y positive upwards and x positive in the flow direction. For the mean velocity contour plot, the magnitude

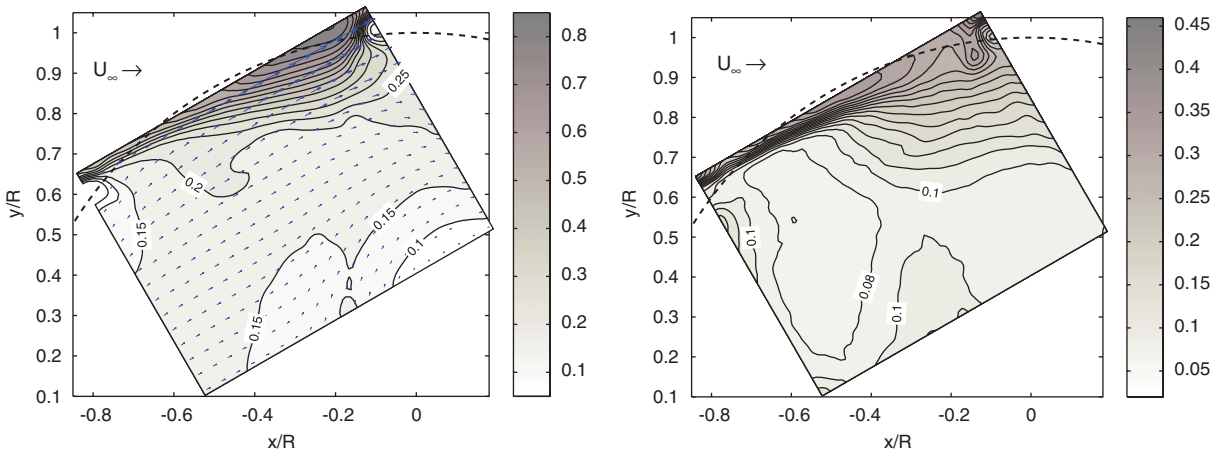

Fig. 9. Velocity mean (left) and r.m.s. (right) obtained from DPIV in region near M2, at a 0° azimuth with respect to the incoming wind and a 35 m s^{-1} freestream velocity without venting. The center of the hemisphere is at $(x, y) = (0, 0)$. Contour intervals are 0.05 for the mean velocity and 0.02 for the r.m.s. velocity, both normalized by the freestream velocity (most labels omitted for clarity). Mean velocity vectors (shown on left-hand plot) all point roughly downstream.

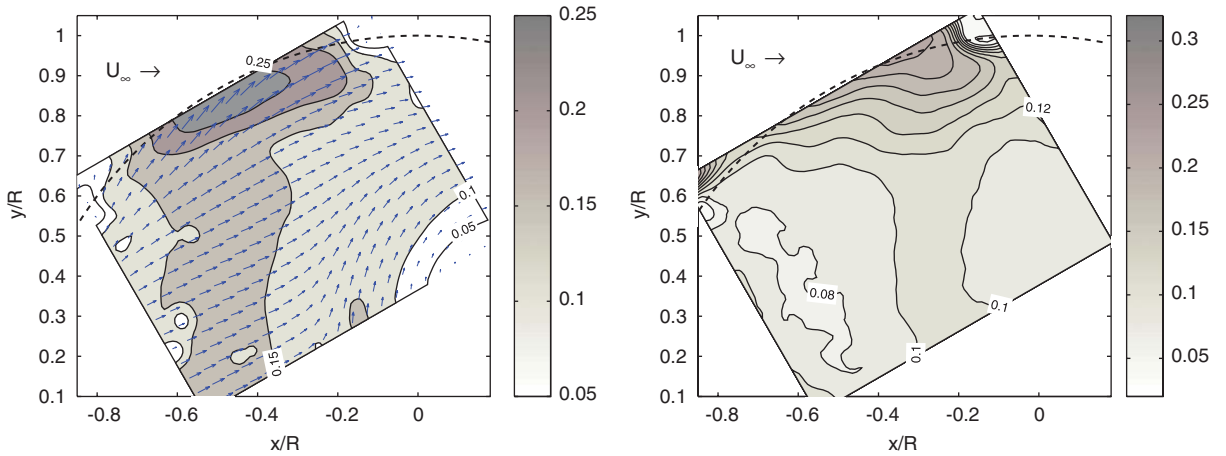

Fig. 10. Velocity mean (left) and r.m.s. (right) obtained from DPIV in region near M2, at a 0° azimuth with respect to the incoming wind and a 19 m s^{-1} freestream velocity.

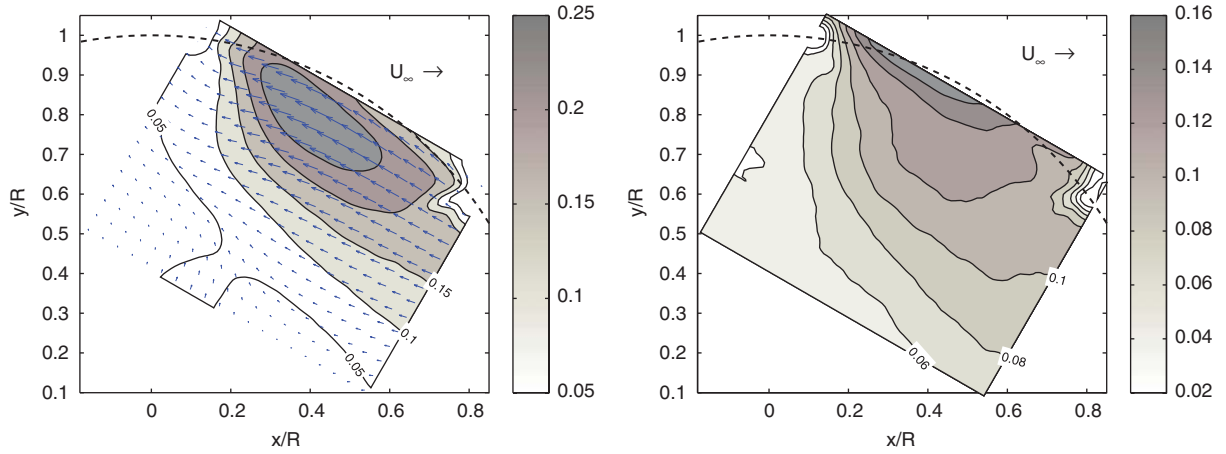

Fig. 11. Velocity mean (left) and r.m.s. (right) obtained from DPIV in region near M2, at a 180° azimuth with respect to the incoming wind and a 35 m s^{-1} freestream velocity without venting; contour intervals as in Fig. 9. Mean velocity vectors point roughly upstream.

of the mean $(|\bar{u}|^2 + |\bar{v}|^2)^{1/2}$ is shown where u and v are the flow components in the x and y direction, with vectors superimposed to show the flow direction (only every 16th vector shown for clarity).

Fig. 9 shows the DPIV data for a 0° azimuth and 35 m s^{-1} wind-tunnel speed. A shear layer exists across the aperture and becomes very thick near the downstream edge of the opening. All of the visible flow is directed generally downstream. The r.m.s. levels are highest in the shear layer, and the elevated r.m.s. levels extend significantly into the enclosure on the downstream half of the opening. A region of upward directed flow with slightly elevated r.m.s. levels exists near the bottom of the field of view ($x/R \sim -0.2$, $y/R \sim 0.4$). This is believed to be due to the triangular base for the hot-wire traverse, directing flow upwards. This portion of the flow field is likely to be entirely different in an enclosure containing a telescope. Decreasing the freestream velocity changes the flow patterns, shown in Fig. 10, because of changes in the shear-layer mode discussed in more detail in the next section.

For a 180° azimuth angle and 35 m s^{-1} speed, shown in Fig. 11, the flow is all generally directed upstream. There is a local maximum in mean velocity magnitude located inside the enclosure. While both the mean and r.m.s. velocity magnitudes are generally lower than in the 0° case, the r.m.s. levels fall off much more gradually inside the enclosure for the 180° case. A region of upward directed flow with slightly elevated r.m.s. levels again exists near the bottom of the field of view ($x/R \sim 0.2$, $y/R \sim 0.4$). The flow in the upstream direction (also evident in flow visualization) indicates that for this azimuth angle, the aperture is inside the region of reversed flow in the enclosure wake.

Data was also collected with 6 of the vent holes shown in Fig. 2 open (corresponding to 12.5% of the area of the aperture), and with all 12 vent holes open. The most significant difference between the flow pattern with vents closed and the flow pattern with vents open is a reduction in the amplitude of the peaks in the spectra, and a corresponding reduction in the r.m.s. velocity measured using DPIV. The righthand plot of Fig. 8 compares the hot-wire spectra at the same speed and orientation with 0 and 6 vent holes open. The mean hot-wire voltage for the two cases differs by a few percent, and thus the (voltage)^4 to velocity calibration for these two cases will also differ. Nonetheless, it is clear that there is a significant reduction in the amplitude of the shear layer modes relative to the broadband amplitude. The broadband turbulence spectrum is essentially unchanged, while the mean-square velocity in the peaks is reduced by roughly a factor of 10. The hot-wire spectrum with all 12 vents open is similar, with a further factor of 3 reduction in the amplitude of the peaks. The mean and r.m.s. unsteady velocity components obtained from DPIV data for a 0° azimuth angle with 6 vents open are shown in Fig. 12. From the hot-wire data, then outside of the shear layer itself, the tones constitute less than 20% of the mean-square velocity for this case, so Fig. 12 gives an indication of the spatial characteristics of the broadband turbulence.

4. Shear layer modes

For the 0° azimuth angle case at 35 m s^{-1}, the smoke visualization clearly indicates the repetitive roll-up of the aperture shear layer into large individual vortices. The hot-wire data demonstrates that this is a periodic roll-up, with a

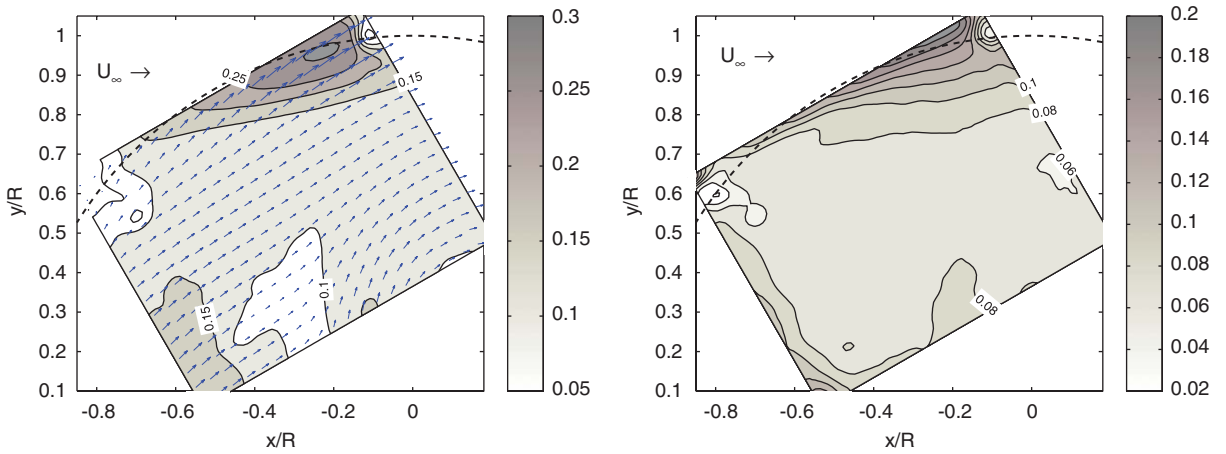

Fig. 12. Velocity mean (left) and r.m.s. (right) obtained from DPIV in region near M2, at a 0° azimuth with respect to the incoming wind and a 35 m s^{-1} freestream velocity with 6 vents open (12.5% of area of viewing slit).

Table 1
Dependence of nondimensional Helmholtz frequency on freestream velocity

U_∞ (m s^{-1})	$\frac{f_H}{f_0}$	$\frac{f_H}{\sigma f_0}$
19	1.06	1.7
35	0.58	0.93

frequency of approximately $0.62f_0$. For lower flow speeds, there is comparable or greater power in the second peak around $1.25f_0$.

A free shear layer is convectively unstable over a range of frequencies and rolls up into large vortex structures. For flow across an open cavity, these vortices interact with the downstream edge of the cavity, propagate upstream as an acoustic pressure wave, and interact with the separating shear layer. This feedback process organizes the flow into distinct modes (Rossiter, 1964). The amplitude of each mode is determined in part by the overall gain of the feedback loop, including both the amplification of the shear layer growth and the acoustic path. The relative amplitude of different modes can therefore depend strongly on the relative amplification of the acoustic path (Rowley et al., 2005).

At the flow speeds of interest in this experiment, the acoustic propagation time in the feedback loop is small, and the temporal frequencies appearing in the flow are well predicted by a single convection speed U_c and the integer number of flow structures n across the opening distance L. Thus,

$$f = n\frac{U_c}{L} = n\sigma f_0, \tag{5}$$

where $\sigma = U_c/U$ is the relative convection speed of the shear layer. Note that at a zenith angle of 30°, the local external velocity across the dome opening will be roughly 30% higher than U_∞. Hence the ratio $\sigma \simeq 0.62$ evident from the hot-wire data is consistent with the expectation that the convection speed is roughly the average velocity of the flow on either side of the shear layer. The convection speed of the vortices is roughly constant over the range of azimuth angles for which peaks in the PSD were observed.

The relative magnitudes of the peaks in the PSD indicate that at different speeds, the number of vortices spanning the enclosure may vary; e.g., at 19 m s^{-1} the $n = 2$ peak is comparable in amplitude to the $n = 1$ peak. The selection of the roll-up mode number, n, is believed to depend on the Helmholtz frequency of the enclosure which acts to increase the feedback gain for any mode which is close in frequency. At the different speeds tested in this experiment, the ratio f_H/f_0 takes on different values, as listed in Table 1. For the highest speed case, $f_H/(\sigma f_0)$ is close to the value corresponding to

$n = 1$, and the first peak in the PSD is dominant (Fig. 7). For $19\,\mathrm{m\,s^{-1}}$, $f_H/(\sigma f_0)$ lies between the frequencies corresponding to $n = 1$ and 2, but is closer to the $n = 2$ frequency. In this case, the second peak in the PSD is comparable to the first peak (Fig. 8), and slightly higher at some locations within the enclosure. This suggests that the Helmholtz frequency is determining the frequency at which the shear layer is actually rolling-up from among the various frequencies compatible with the convection velocity. For the full-scale enclosure in $12\,\mathrm{m\,s^{-1}}$ winds, $f_H/(\sigma f_0)$ would be approximately 2.8, so one would expect to see an $n = 3$ type roll-up of the shear layer. At lower wind speeds, f_H/f_0 would be even larger, so higher modes could be expected.

In the data taken with vents open, the frequencies of the shear layer modes remains the same, but the amplitude decreases significantly, as noted previously in the righthand plot of Fig. 8. The reduction in shear layer mode amplitude is believed to result from significantly increased damping of the Helmholtz mode with even small amounts of open area, and thus less amplification. Thus an important conclusion from this data is that the unsteady loads on the secondary mirror and secondary support structure may be reduced by opening vents on the enclosure. The overall amplitude of the shear layer mode will also depend on any external structure near the dome opening that interferes with the development of the spanwise vortex roll-up.

The mean and r.m.s. velocity fields observed with DPIV for 0° azimuth angle are consistent with the roll-up of vortices evident in the flow visualization and hot-wire data. At $35\,\mathrm{m\,s^{-1}}$ without venting, the first peak at $0.62f_0$ is dominant in all of the hot-wire data. From Fig. 9, the shear layer appears thick in the mean flow and the r.m.s. magnitude is large deep inside the dome on the downstream side of the opening due to the formation of the large vortices. For a $19\,\mathrm{m\,s^{-1}}$ wind-tunnel speed the $n = 1$ tone is weaker and the second tone at $1.25f_0$ is the larger tone at some locations within the enclosure, consistent with the images from Fig. 6. Fig. 10 shows lower r.m.s. magnitudes on the downstream side of the opening, and a reduced extent into the dome from the vortices. As noted earlier, for the data taken with vents open (Fig. 12) the r.m.s. velocity is primarily due to the broadband turbulence. The r.m.s. levels are still higher on the downstream side of the opening, but the penetration into the enclosure is the least of all the 0° azimuth cases.

For azimuth angles greater than 90°, such as the 180° case in Fig. 11, there is no strong shear layer over the aperture, and therefore no significant peaks in the PSD of the hot-wire signals.

5. Effects on the secondary mirror

For determining the effects on M2 and nearby supporting structure, it is useful to consider the mean and r.m.s. in-plane velocity magnitude profiles along the telescope axis. This is extracted from the DPIV data and shown in Fig. 13 for the 0° azimuth case at 35 and $19\,\mathrm{m\,s^{-1}}$, at $35\,\mathrm{m\,s^{-1}}$ with 6 vents open, and for the 180° azimuth case at $35\,\mathrm{m\,s^{-1}}$. For all of the 0° cases, both the mean and r.m.s. magnitudes are relatively constant deep inside the enclosure, but increase sharply in the shear layer. This suggests that it may be beneficial to design an enclosure that results in M2 being located deep enough inside that dome that it is not sitting in the shear layer. As the mode number n increases, the radius of the vortices should decrease. The depth into the dome which the region of high mean velocities and high r.m.s. magnitudes extends will therefore be smaller for lower flow speeds typical of the full-scale enclosure. For the worst-case of an unvented enclosure with the $n = 1$ mode dominant, the increase in mean and r.m.s. occurs at about 80% of the radius. At $19\,\mathrm{m\,s^{-1}}$, the increase occurs at 85% of the radius. With the vents open, the amplitude of the shear layer modes drops significantly, and the residual r.m.s. is primarily due to the broadband turbulence. Thus this case, where the increase occurs at nearly 90% of the radius, represents the best that can be expected. For this dome geometry, this critical radius is only slightly inside the line connecting the upstream and downstream edges of the aperture; this line crosses the telescope axis at a radius $[R^2 - (L/2)^2]^{1/2} = 0.92R$. If the telescope structure is small compared to the flow so that it does not significantly influence the flow patterns, then the pressure on the structure can be estimated from $p = \frac{1}{2}\rho u^2$. If the mean velocity $\bar{u}$ is large compared to the fluctuating component u', then the fluctuating component of the pressure is roughly $p' = \frac{1}{2}\rho(2\bar{u}u')$. The velocity data along the telescope axis can then be used to estimate loads on the secondary mirror and nearby support structure, with the broadband turbulence and shear layer mode components separately estimated from the data with and without the vents open. A preliminary analysis is presented in MacMynowski et al. (2004).

The mean and r.m.s. velocity magnitude profiles along the telescope axis are also plotted for the 180° azimuth case in Fig. 13. While the maximum mean and r.m.s. velocity magnitudes are smaller for this case than for the 0° case, high levels of fluctuations extend deeper into the enclosure. The local maximum in mean velocity magnitude is due to the change in flow direction between the wake region and the outer flow—there is a shear layer located above the enclosure across which the flow reverses direction, so the mean velocity magnitude must go to zero somewhere in that shear layer.

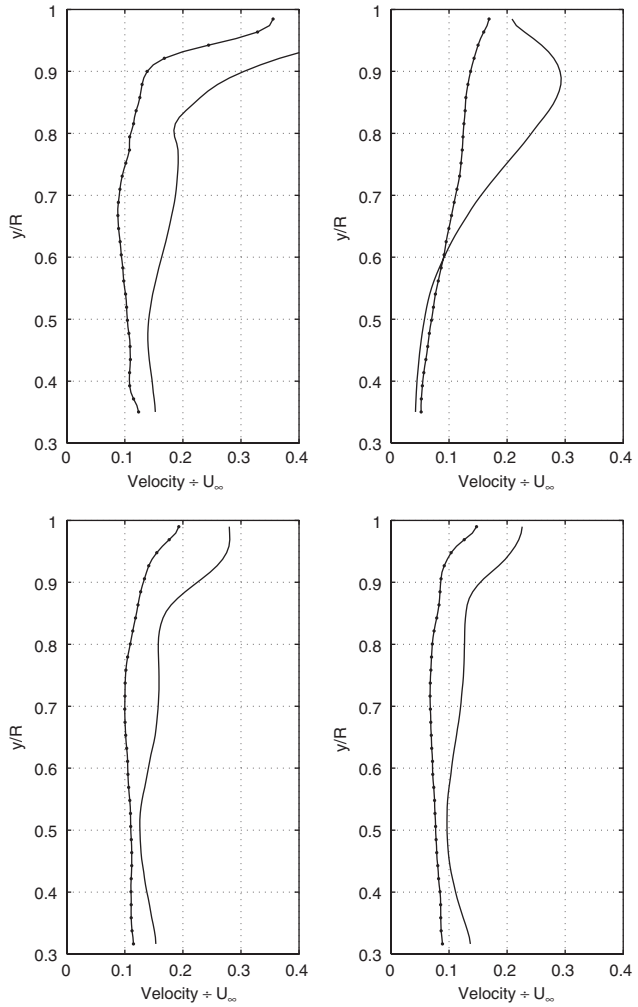

Fig. 13. Velocity mean (solid) and r.m.s. ('·') along telescope axis, normalized by the freestream velocity. From left to right on top row, (i) 0° azimuth at 35 m s^{-1} with no vents, (ii) 180° azimuth at 35 m s^{-1} with no vents, and bottom row, (iii) 0° azimuth at 19 m s^{-1} with no vents, (iv) 0° azimuth at 35 m s^{-1} with 6 vents open.

6. Conclusions

Two very different types of flow inside of a telescope enclosure exist depending on the azimuth angle of the aperture with respect to the wind, the wind velocity, and the vented area of the enclosure.

For upwind viewing, there is a strong shear layer over the telescope aperture. This shear layer drives the flow inside the enclosure. The shear layer rolls up periodically into vortices which can extend inside the enclosure and may produce significant unsteady forces on the secondary mirror and supporting structure. The frequency at which the shear layer rolls up is well described by a convective velocity, determined to be about $0.62U_\infty$, and a mode number corresponding to the number of vortices spanning the aperture at one time. The particular mode that is excited is determined by the Helmholtz resonance. Including even small amounts of open venting on the enclosure significantly reduces the amplitude of these shear layer modes. Additional external features on a full-scale enclosure will also affect the shear layer roll-up.

For downwind viewing, the aperture is located inside the wake of the enclosure. This results in reversed flow in the wake driving the flow inside the enclosure. In this configuration, there are no significant large scale unsteady flow structures. However, the broadband turbulence in the flow may still produce significant forces on the telescope. For both upwind and downwind viewing, the broadband turbulence spectrum is roughly of von Karman type.

The data obtained from this test are being used to validate CFD studies of air flow in telescope enclosures (Vogiatzis et al., 2004) and to develop models of the wind loads for use in telescope structural designs (MacMynowski et al., 2004).

Acknowledgments

The Thirty Meter Telescope (TMT) Project is a partnership of the Association of Universities for Research in Astronomy (AURA), the Association of Canadian Universities for Research in Astronomy (ACURA), the California Institute of Technology and the University of California. The partners gratefully acknowledge the support of the Gordon and Betty Moore Foundation, the US National Science Foundation, the National Research Council of Canada, the Natural Sciences and Engineering Research Council of Canada, and the Gemini Partnership.

Mory Gharib at Caltech provided substantial guidance and technical expertise in the design of this experiment and the application of the DPIV technique. Christopher Krok and Jerry Landry from the Lucas AWT at Caltech supplied technical assistance in the areas of model construction, flow visualization, troubleshooting and test documentation. Joeleff Fitzsimmons from HIA and Konstantinos Vogiatzis from AURA provided insight and consulted on the selection of test conditions.

References

Adrian, R.J., 1991. Particle-imaging techniques for experimental fluid mechanics. Annual Review of Fluid Mechanics 23, 261–304.

Angeli, G.Z., Cho, M.K., Sheehan, M., Stepp, L.M., 2002. Characterization of wind loading of telescopes. In: Andersen, T. (Ed.), Proceedings of the SPIE, vol. 4757; Workshop on Integrated Modeling of Telescopes, pp. 72–83.

Angeli, G.Z., Roberts, S., MacMynowski, D.G., Fitzsimmons, J., Dunn, J., Vogiatzis, K., 2004. Modeling tools to estimate the performance of the Thirty Meter Telescope: an integrated approach. In: Craig, S.C., Cullum, M.J. (Eds.), Proceedings of the SPIE, vol. 5497; Modeling and Systems Engineering for Astronomy, pp. 237–250.

Beranek, L.L., 1954. Acoustics. Acoustical Society of America.

Cho, M.K., Stepp, L.M., Angeli, G.Z., Smith, D.R., 2002. Wind loading of large telescopes. In: Oschmann, J., Stepp, L.M. (Eds.), Large Ground-Based Telescopes, Proceedings of the SPIE, vol. 4837, pp. 352–367.

DeYoung, D.S., 1996. Numerical simulations of airflow in telescope enclosures. The Astronomical Journal 112 (6), 2896–2908.

Fitzsimmons, J., Dunn, J., Herriot, G., Jolissaint, L., Roberts, S., Mamou, M., Cooper, K., 2004. Predicting the aerodynamic performance of the Canadian Very Large Optical Telescope. In: Craig, S.C., Cullum, M.J. (Eds.), Proceedings of the SPIE, vol. 5497; Modeling and Systems Engineering for Astronomy, pp. 321–328.

Forbes, F., Gabor, G., 1982. Wind loading of large astronomical telescopes. In: Proceedings of the SPIE, vol. 332; Advanced Technology Telescopes, pp. 198–205.

Kiceniuk, T., Potter, K., 1986. Internal air flow patterns for the Keck 10 meter telescope observatory dome. Keck Observatory Report # 166.

Lamarche, L., Wedemeyer, E., 1984. Minimization of wall interference for three dimensional models with two dimensional wall adaptation. Technical Report 149, von Karman Institute for Fluid Dynamics.

MacMynowski, D.G., Angeli, G.Z., Vogiatzis, K., Fitzsimmons, J., Padin, S., 2004. Parametric modeling and control of telescope wind-induced vibration. In: Craig, S.C., Cullum, M.J. (Eds.), Proceedings of the SPIE, vol. 5497; Modeling and Systems Engineering for Astronomy, pp. 266–277.

McKenna, S.P., McGillis, W.R., 2002. Performance of digital image velocimetry processing techniques. Experiments in Fluids 32, 106–115.

Padin, S., Davison, W., 2004. Model of image degradation due to wind buffeting on an extremely large telescope. Applied Optics 43 (3), 592–600.

Ravensbergen, M., 1994. Main axes servo systems of the VLT. In: Stepp, L.M. (Ed.), Proceedings of the SPIE, vol. 2199; Advanced Technology Optical Telescopes V, pp. 997–1005.

Riewaldt, H., Lastiwka, M., Quinlan, N., McNamara, K., Wang, X., Andersen, T., Shearer, A., 2004. Wind on the Euro50 enclosure. In: Antebi, J., Lemke, D. (Eds.), Proceedings of the SPIE, vol. 5495; Astronomical Structures and Mechanisms Technology, pp. 537–548.

Rossiter, J.E., 1964. Wind-tunnel experiments on the flow over rectangular cavities at subsonic and transonic speeds. Aeronautical Research Council Reports and Memoranda, No. 3438.

Rowley, C.W., Williams, D.R., Colonius, T., Murray, R.M., MacMynowski, D.G., 2005. Linear models for control of cavity flow oscillations. Journal of Fluid Mechanics, to appear.

Schneermann, M., 1994. VLT enclosures wind tunnel tests and fluid dynamic analyses. In: Stepp, L.M. (Ed.), Proceedings of the SPIE, vol. 2199; Advanced Technology Optical Telescopes V, pp. 465–476.

Sears, W.R., Erickson, J.C., 1988. Adaptive wind tunnels. Annual Review of Fluid Mechanics 20, 17–34.

Srinivasan, G.R., 2000. Acoustics and unsteady flow of telescope cavity in an airplane. Journal of Aircraft 37 (2), 274–281.

Vogiatzis, K., Segurson, A., Angeli, G.Z., 2004. Estimating the effect of wind loading on extremely large telescope performance using computational fluid dynamics. In: Craig, S.C., Cullum, M.J. (Eds.), Proceedings of the SPIE, vol. 5497; Modeling and Systems Engineering for Astronomy, pp. 311–320.

Willert, C.E., Gharib, M., 1991. Digital particle image velocimetry. Experiments in Fluids 10, 181–193.